ACS APPLIED MATERIALS & INTERFACES

Research Article

www.acsami.org

Nitrogen-Doped Porous Carbons As Electrode Materials for High-Performance Supercapacitor and Dye-Sensitized Solar Cell

Lan Wang, Zhiyong Gao,* Jiuli Chang, Xiao Liu, Dapeng Wu, Fang Xu, Yuming Guo, and Kai Jiang*

School of Chemistry and Chemical Engineering, Collaborative Innovation Center of Henan Province for Green Manufacturing of Fine Chemicals, Key Laboratory of Green Chemical Media and Reactions, Ministry of Education, Henan Normal University, Henan, Xinxiang 453007, P.R. China

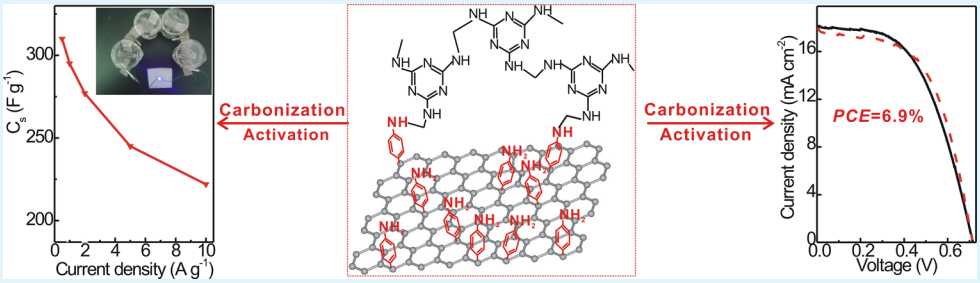

ABSTRACT: Activated N-doped porous carbons (a-NCs) were synthesized by pyrolysis and alkali activation of graphene incorporated melamine formaldehyde resin (MF). The moderate N doping levels, mesopores rich porous texture, and incorporation of graphene enable the applications of a-NCs in surface and conductivity dependent electrode materials for supercapacitor and dye-sensitized solar cell (DSSC). Under optimal activation temperature of 700 °C, the afforded sample, labeled as a-NC_{700}, possesses a specific surface area of 1302 m^2 g^{-1}, a N fraction of 4.5%, and a modest graphitization. When used as a supercapacitor electrode, a-NC_{700} offers a high specific capacitance of 296 F g^{-1} at a current density of 1 A g^{-1}, an acceptable rate capability, and a high cycling stability in 1 M H_2SO_4 electrolyte. As a result, a-NC_{700} supercapacitor delivers energy densities of 5.0−3.5 Wh kg^{-1} under power densities of 83−1609 W kg^{-1}. Moreover, a-NC_{700} also demonstrates high electrocatalytic activity for I_3^- reduction. When employed as a counter electrode (CE) of DSSC, a power conversion efficiency (PCE) of 6.9% is achieved, which is comparable to that of the Pt CE based counterpart (7.1%). The excellent capacitive and photovoltaic performances highlight the potential of a-NCs in sustainable energy devices.

KEYWORDS: *N-doped porous carbons, graphene, melamine formaldehyde resin, supercapacitor, dye-sensitized solar cell*

1. INTRODUCTION

With the ever-growing energy consumption and the concomitant environmental issues due to urbanization worldwide, efficient, sustainable, and green energy forms are highly demanded. Supercapacitors and DSSCs are intriguing energy forms sharing the merits of high performances, low costs, and eco-benign fabrications. In both energy source forms, electrode material is the key component determining the overall performance, so the exploration of efficient electrode materials has aroused great investigation enthusiasm. Carbon materials are the most popular electrode materials of supercapacitors and DSSCs owing to their good conductivities, high surface areas, and intrinsic chemical inertness against corrosive electrolyte. In term of supercapacitors, various carbon materials including activated carbons,[1,2] graphene,[3−5] and carbon nanotubes[6,7] were widely employed as electrode materials to offer electrical double layer (EDL) capacitance by virtue of the high surface areas. Whereas for catalytic CE of DSSC, the edges and defect sites within the graphitic carbon matrix can function as active sites toward the redox of iodide mediator in electrolyte and further result in a high PCE. In all, the EDL capacitances of pure carbon electrode materials are insufficient merely rely on physical charge storage, and the PCE of DSSC based on carbon CE is also relatively low owing to the low defect sites within the carbon matrix.

Recent investigations have demonstrated that N-doped porous carbons are promising materials of supercapacitors for increased wettability and additional pseudocapacitance stemming from redox conversion of N functionalities while maintaining good cycling stabilities.[8,9] Besides, due to the higher electronegativity of N (χ = 3.04) relative to C (χ = 2.55),[10,11] the incorporation of N atoms into the carbon matrix creates positive charge of the carbon atoms adjacent to the doped N, which endows these carbon atoms with metallic catalytic activity for certain redox reactions[12−14] or oxygen reduction reaction in alkaline media.[15] The lone pair electrons of pyridinic and pyrrolic N can also function as electron donor boosting the catalytic activity on I_3^- reduction,[16,17] so the applications of N-doped porous carbons in Pt-free catalytic CEs of DSSCs were also extensively investigated and obviously

Received: June 29, 2015
Accepted: August 31, 2015
Published: August 31, 2015

DOI: 10.1021/acsami.5b05790
ACS Appl. Mater. Interfaces 2015, 7, 20234−20244

improved photovoltaic performances were achieved.[10,11,18,19] Hence, the design of efficient N-doped porous carbon is meaningful for enhancing the performances of both supercapacitor and DSSC.

In general, the synthesis approaches toward N-doped porous carbon mainly include the carbonization and activation of N-containing precursors, as well as the passivation of carbon matrix by reactive nitrides. Among both pathways, the former is more preferable for the simple and scalable synthesis process. Many N-containing chemicals were widely employed as precursors for preparation of N-containing porous carbons to improve the electrochemical performances.[18,20−24] As for N-doped carbons, the N level directly determines the electrochemical performances, so the N-rich organics are accepted as more preferable precursors for high-performance N-doped carbons. Melamine is a N-rich organics for the modification of three amino groups onto the triazine ring, which can react with aldehydes to form resins with high N level and function as promising precursors toward N-doped porous carbons for application in supercapacitors and DSSCs.[18,24−26] MF resin is the most common melamine-related polymer, which is an ideal C and N source toward N-doped carbons; the pyrolysis of MF can generate rich pores within the C−N framework via structural contraction and the release of thermo-decomposed gases.[25] On the other hand, graphene is an ultrathin 2-dimensional carbon material with extraordinary conductivity, huge surface area, and robust mechanical strength; these characteristics are beneficial for enhancing conductivity, structural stability of electrode materials, and therefore the improved electrochemical performances of graphene-based composites. Therefore, the capacitive and photovoltaic performances of graphene-incorporated N-containing porous carbon in supercapacitor and DSSC are worth expecting.

Herein, graphene-incorporated MF resin via covalent bonding was synthesized and further adopted as a precursor toward a-NCs with N-rich porous texture. The electrochemical performances of the as-prepared a-NCs in electrode material of supercapacitor and DSSC were assessed. Under optimal synthesis condition, a-NC_{700} offers high electrochemical capacitance when employed as a supercapacitor electrode, and competitive photovoltaic performance is also achieved by application as a catalytic CE of DSSC.

2. EXPERIMENTAL SECTION

Synthesis of NC. Aniline-modified graphene (a-G) was synthesized by diazotization modification of *p*-phenylenediamine onto reduced graphene oxide;[27] in brief, equal molar of *p*-phenylenediamine and $NaNO_2$ were dissolved into acidic media containing reduced graphene oxide under ice bath to covalently anchor the formed reactive aryl cations onto the carbon matrix. In the synthesis of graphene−MF resin composite, 10 mg of a-G was initially dispersed in 10 mL of deionized water. Subsequently, 1 g of melamine and 1.8 g of 37% formaldehyde were added into the a-G suspension; the pH of the solution was adjusted to ca. 8 using diluted NaOH solution. After being ultrasonicated for 10 min to ensure a homogeneous suspension, the reaction mixture was transferred into a 50 mL Teflon-lined autoclave and subjected to heating at 140 °C for 4 h to form graphene-incorporated MF resin. After being washed copiously with deionized water and dried overnight at 80 °C, the graphene−MF resin composite was calcinated at 800 °C for 2 h in N_2 atmosphere; the afforded N-doped porous carbon was labeled as NC.

Synthesis of a-NCs. For the activation treatment, NC was dipped into KOH aqueous solution with a NC-to-KOH mass ratio of 1:3. Then, the mixture was dried at 80 °C overnight. The dry mixture was placed into a tube furnace, heated to the target temperature (500, 600, 700, or 800 °C) at a rate of 5 °C min^{-1}, and maintained for 2 h under N_2 atmosphere. After being cooled down, the products were washed thoroughly with 1 M HCl and deionized water and dried for structural characterizations and electrochemical measurements. The resultant samples were labeled as a-NC_{500}, a-NC_{600}, a-NC_{700}, and a-NC_{800}, respectively, according to activation temperature.

Characterizations. Morphological and structural features of the materials were characterized by scanning electron microscopy (SEM, JEOL JSM-6390) and high-resolution transmission electronic microscopy (HRTEM, JEOL JEM-2100). X-ray diffraction (XRD, Bruker D8 Advance diffractometer with Cu Ka radiation) was used for phase analyses. Raman spectra were measured on JOBIN YVON HR800 Confocal Raman spectrometer with 632.8 nm laser excitation. Chemical compositions of the samples were evaluated by X-ray photoelectron spectroscopy (XPS, Thermo Fisher ESCALab 250 X-ray photoelectron spectrometer with Al Ka radiation). N_2 sorption isotherms were measured on a Micromeritics Gemini2380 surface area analyzer at 77 K; the specific surface areas and pore size distributions of the samples were calculated based on Brunauer−Emmett−Teller (BET) model and nonlocal density functional theory (NLDFT). The wettabilities of NC and a-NC_{700} were compared by water contact angle measurements; the water pearls dropped onto the surface of NC and a-NC_{700} based capacitor electrodes were imaged within 5 s.

Electrochemical Measurements. In capacitive performance measurements, the work electrodes were fabricated by coating slurry containing 85 wt % active material, 10 wt % acetylene black, and 5 wt % polytetrafluoroethylene binder onto stainless steel net collector (500 mesh). Cyclic voltammetry (CV) and electrochemical impedance spectroscopy (EIS) of the supercapacitor electrodes were performed on CHI 660D electrochemical workstation (Chenhua Instrument). The three-electrode test system for CV measurement includes an active material-loaded working electrode, a platinum wire auxiliary electrode, and a Ag/AgCl reference electrode immersed in 1 M H_2SO_4 electrolyte over the potential range of 0−0.7 V at scan rates of 10−100 mV s^{-1}. In EIS measurements, impedances of symmetric capacitors were recorded within 10^5−0.01 Hz at open circuit potential with an ac perturbation of 5 mV. Galvanostatic charge−discharge (GCD) curves of symmetric supercapacitors were measured in double-electrode configuration. The specific capacitance (C_s, F g^{-1}) of single electrode, energy densities (E_{cell}, Wh kg^{-1}), and power densities (P_{cell}, W kg^{-1}) of symmetric supercapacitors were calculated from GCD measurements according to the following equations:

$$C_s = 2I\Delta t/(\Delta V \times m) \quad (1)$$

$$E_{cell} = C_s(\Delta V - IR)^2/8 \quad (2)$$

$$P_{cell} = E_{cell}/\Delta t \quad (3)$$

where I (A) is the discharge current, ΔV (V) and Δt (s) represent voltage and discharge duration, respectively, IR is the voltage drop from inner resistance at the initial stage of discharge process, and m (g) is the weight of active material on each electrode.

In electrochemical measurements of a-NC_{700} based CE of DSSC, the CE was fabricated by coating a-NC_{700} onto clean fluorine-doped tin oxide (FTO) substrate with a thickness of 12 μm using tape as the frame. Pt CE was fabricated by pyrolysis of dip-coated H_2PtCl_6 onto FTO substrate. CVs of CEs were also measured on the same CHI 660D workstation; the three-electrode test system includes a Pt wire auxiliary electrode, a Ag/AgCl reference electrode, and an a-NC_{700}/FTO or Pt/FTO working electrode dipped in an acetonitrile electrolyte containing 10 mM LiI, 1 mM I_2, and 0.1 M $LiClO_4$. EIS plots of the symmetric cells composed of two identical electrodes were also measured in the same electrolyte. DSSC was fabricated by sandwiching of a CE and a porous TiO_2 microsphere photoanode sensitized by N719 dye (12 μm in thickness), an acetonitrile electrolyte composed of 0.3 M 1,2-dimethyl-3-propylimidazolium iodide (DMPII), 0.5 M LiI, 0.05 M I_2, and 0.5 M 4-*tert*-butylpyridine was filled into the cell. Photocurrent−voltage (J−V) curves of the DSSCs were measured on a Keithley 2400 sourcemeter under

DOI: 10.1021/acsami.5b05790
ACS Appl. Mater. Interfaces 2015, 7, 20234−20244

Scheme 1. Illustration of the Formation Procedure Toward (1) MF Resin and (2) Graphene−MF Composite

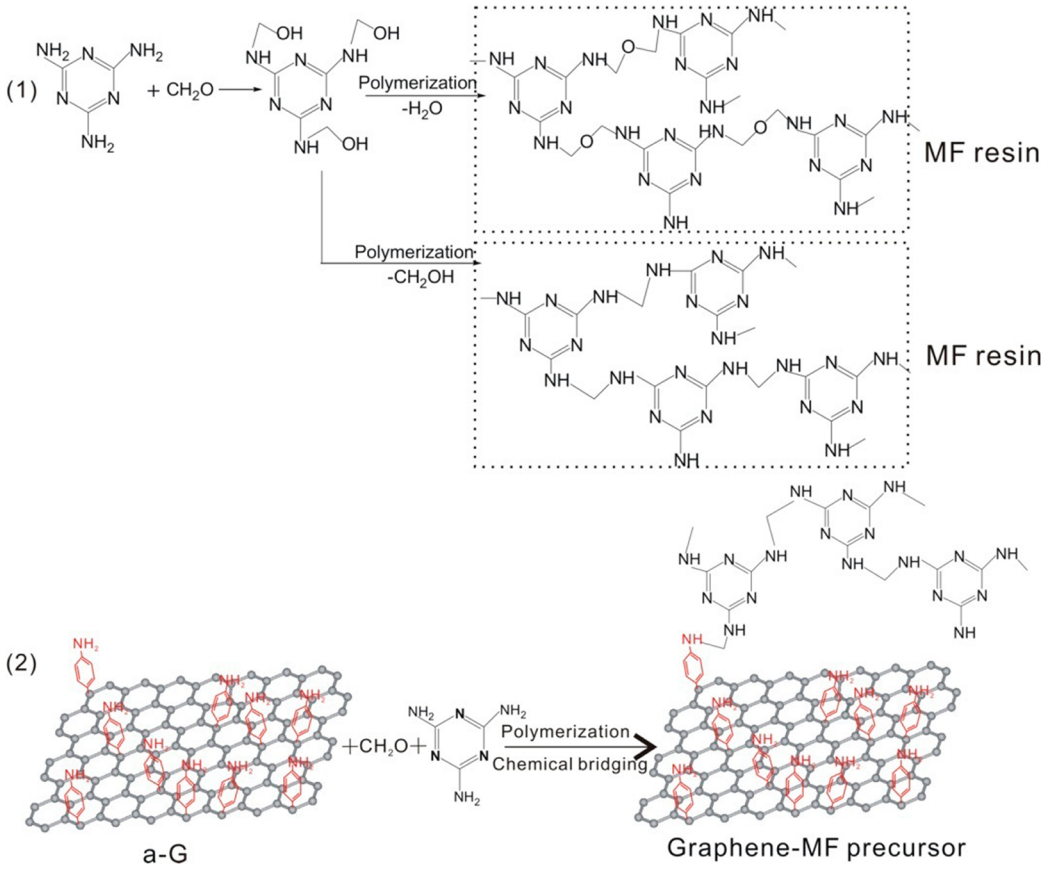

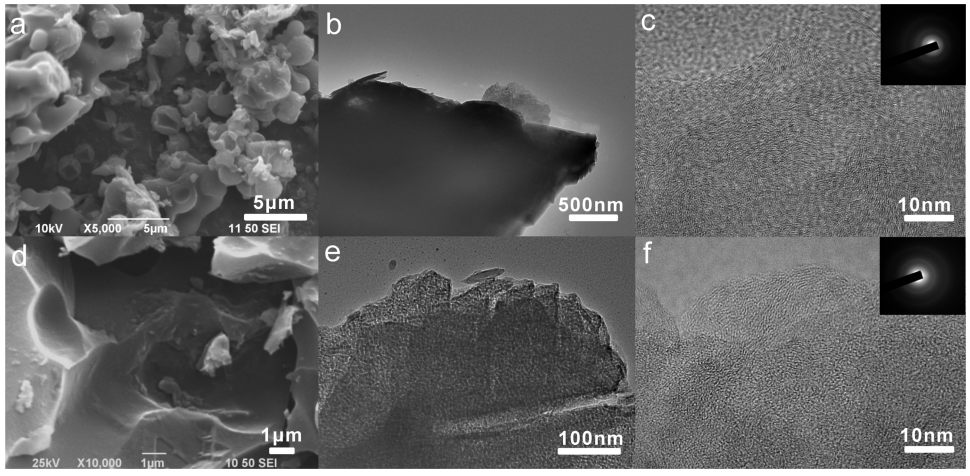

Figure 1. SEM (a, d) and TEM (b, c, e, f) of NC (a−c) and a-NC_{700} (d−f) at different magnifications. Inset in panels c and f: selected area electron diffraction (SAED) of NC and a-NC_{700}.

illumination power density of 100 mW cm^{-2} (AM 1.5) from a Newport xenon lamp solar simulator.

3. RESULTS AND DISCUSSION

Formation of Graphene−MF Resin Composite. a-NCs were prepared by the pyrolysis and alkali activation of graphene−MF resin composite, which was synthesized by incorporation of a-G into the MF formation system via chemical bridging. As shown in Scheme 1, the nucleophilic attack of melamine to formaldehyde causes the methylolation of melamine; the following dehydration and partial demethylol of methylolated melamine trigger the polymerization and condensation toward MF resin.[28,29] By incorporation of a-G, the amine groups in functionalized aniline serve as nucleophilic sites to attack the carbonyl carbon atom of formaldehyde to accomplish methylolation in a similar mode. The subsequent dehydration and partial demethylol reaction results in the ether and methylene bonds linkage to the formed MF polymer. By this means, the covalent bridging between graphene and MF resin affords stable graphene−MF resin composite with homogeneous incorporation of graphene. Due to the high nitrogen level (67% N mass fraction) of melamine unit, the

DOI: 10.1021/acsami.5b05790
ACS Appl. Mater. Interfaces 2015, 7, 20234−20244

prepared graphene−MF composite can be employed as an ideal precursor for fabrication of NC with a high N doping level. Besides, the covalent bridging of flexible and highly conductive graphene to MF resin enables the construction of multidimensional conductive channels and possibly enhances the overall conductivity of the final a-NCs. Moreover, the alkali activation creates rich pores and hydrophilic surface by etching the NC framework. Hence, a-NCs with the incorporation of graphene in this manner facilitate the applications as electrode materials of supercapacitors and DSSCs for the desired factors including large surface area, moderate conductivity, essential redox active sites and good electrolyte ions compatibility can be achieved simultaneously.

Morphological and Structural Characterizations. Figure 1 compares the morphology and microstructure of NC and the typical a-NC_{700} sample; from Figure 1a, the morphology of NC includes fused microspheres and some scattered shells. Generally, MF resin exhibits discrete microspheres without morphology-directing reagents;[25] the fused morphology is mainly attributed to the embedded graphene, which act as anchoring sites directing the condensation of MF resin onto the graphene sheet, thus causes the stacking and fusion of the MF microspheres with irregular shape. The formation of isolated shells is not clear, which is presumably formed by the encircling of the high amount of thermal decomposed gases by the fusion CN wall at high carbonization temperature, which is reported to be formed by carbonization temperature over 700 °C.[25] Energy-dispersive X-ray spectroscopy (EDX) elemental mapping of NC (Figure 2) reveals the composing of C, N, and O

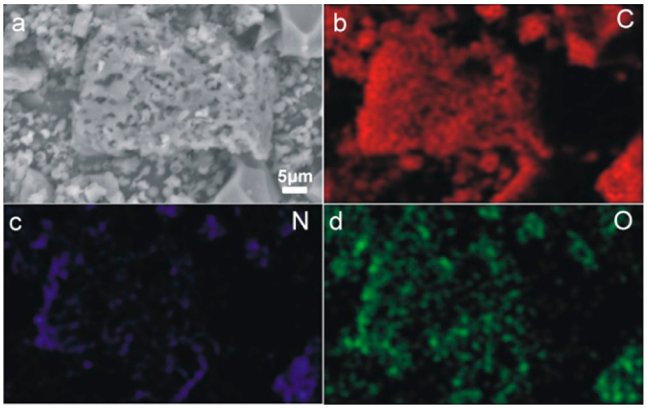

Figure 2. EDS mapping images of NC: (a) SEM image; (b) C, (c) N, and (d) O elemental distributions.

elementals. All the three elementals are homogeneously scattered across the sample, indicating the homogeneous distribution of N elemental throughout the carbon framework. The N content is estimated to be 12%, showing the advantage of graphene−MF composite in NC preparation. TEM image (Figure 1b) of NC fragment reveals the dark body with high contrast against the background, showing the high density of NC. From HRTEM (Figure 1c), the curl and discontinuous fringes are typical characteristics of the carbon material, indicating the formation of numerous tiny graphitization regions by pyrolysis. After molten KOH activation, the outer surface of a typical a-NC_{700} sample exhibits irregular big blocks with obvious edges (Figure 1d), which may be due to the etching and cutting of the NC surface by alkali activation. The TEM image more clearly reveals the structural change by activation, as observed from Figure 1e; the transparency of a-NC_{700} is much higher, which comprises numerous mesopores, further evidences the much hollowed texture. The HRTEM (Figure 1f) image reveals the presence of rich fringes at the rim of the sample, indicating the still maintaining of graphitized microregions after activation treatment. As compared with NC, more micropores and mesopores are produced by this alkali activation step, therefore substantially increases the surface area and porosity, which further favors the application as surface-dependent electrode material of supercapacitor and DSSC. Selected-area electron diffraction (SAED) patterns of NC and a-NC_{700} (inset in panels c and f) show ambiguous rings, revealing the largely amorphous nature of NC and a-NC_{700}.

The phase and structure of NC and a-NCs are revealed by XRD, as shown in Figure 3a; all the samples feature a weak and broad peak at 26°, which is indexed to the (002) plane reflection of graphitic carbon, the wide band and the low intensity indicate the less-ordered stacking of graphite layers because of the smaller graphitic regions and the local lattice distortion by N doping. Besides, the rich pores also disturb the stacking periodicity of the graphitic carbon layer. Another diffraction at 43° stemming from (101) plane emerges for a-NC_{800}, showing the increased lattice periodicity within the basal graphene plane. Hence, higher activation temperature is beneficial for increased crystallinity. As a whole, the weak diffraction intensities of both peaks suggest the largely amorphous phase of all samples. Figure 3b shows Raman spectra of NC and a-NCs; all the samples exhibit two peaks located at 1330 (D band) and 1578 cm^{-1} (G band). The D band arises from the A_{1g} vibration of structural defects and partially disordered structures resulting from the low crystallinity and the presence of heteroatoms in the carbon framework, whereas the G band corresponds to the E_{2g} symmetric vibration mode of graphitic carbon. The D band-to-G band intensity ratios (I_D/I_G) are 1.21, 1.26, 1.25, 1.21, and 1.20, respectively, for NC, a-NC_{500}, a-NC_{600}, a-NC_{700}, and a-NC_{800}, the gradual decrement of I_D/I_G at higher activation temperature reflects the slightly increased crystallinity,[30] which agrees with the XRD result. The chemical compositions of NC and a-NC_{700} sample were characterized by XPS; from Figure 3c, both samples comprise three peaks located at 285, 400, and 532 eV, which are assigned to C 1s, N 1s, and O 1s spin orbits, evidence of the coexistence of C, N, and O elementals. Relative to NC, the N fraction of a-NC_{700} decreases to 4.5% (Table 1), which can be evidenced by the decrease of the N 1s peak while the O 1s peak increases. Due to the lower bonding energy of the C−N bond (305 kJ mol^{-1}) versus the C−C bond (370 kJ mol^{-1}),[31] the C−N bond is more vulnerable to cleavage and causes partial N loss when it undergoes high-temperature activation. Simultaneously, O is introduced by alkali activation and thus results in decreased N but increased O. Deconvolution of C 1s peak for NC shows the presence of C═C (284.7 eV), C−N/C−O−C (285.5 eV), and C═O (286.7 eV) bonds;[32] the high intensities of the former two peaks indicate the presence of a high fraction of N in the C═C framework of NC (left inset). The N 1s peak mainly includes pyridinic- (398.1 eV), pyrrolic- (400.3 eV), and a low fraction of graphitic N (401.6 eV) (right inset), thus showing that the N heteroatoms in NC predominate in pyridinic and pyrrolic forms.[33,34] By alkali activation, the C−N/C−O−C intensity increases in a-NC_{700} (Figure 3d); considering the decreased N fraction, the activation mainly generates rich ether bonds in the carbon framework. Additionally, the graphitic N also increases (inset),

DOI: 10.1021/acsami.5b05790
ACS Appl. Mater. Interfaces 2015, 7, 20234−20244

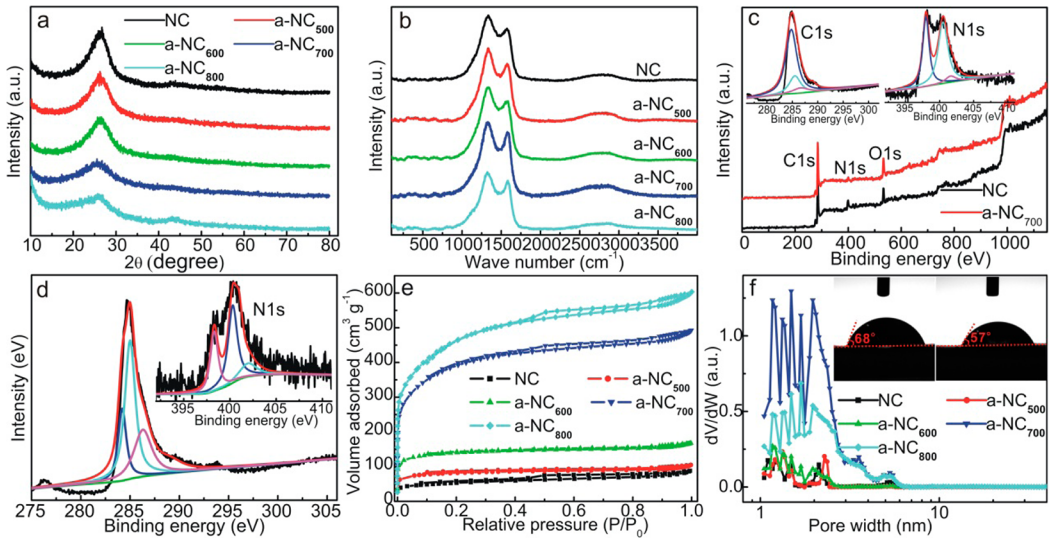

Figure 3. (a) XRD patterns and (b) Raman spectra of NC and a-NCs. (c) XPS of NC and a-NC_{700}; inset: C 1s and N 1s of NC. (d) C 1s and N 1s of a-NC_{700}. (e) N_2 sorption isotherms and (f) NLDFT pore size distributions of NC and a-NCs; inset: contact angles of NC (left) and a-NC_{700} (right).

Table 1. Textural Parameters, Surface N Contents, and States of NCs and a-NCs[a]

					N states (%)		
samples	S_{BET} (m^2 g^{-1})	S_{micro} (m^2 g^{-1})	V_{total} (cm^3 g^{-1})	atomic N content (%)	pyridinic-	pyrrolic-	graphitic-
NC	172.1	143.2	0.14	11.7	40.8	44.4	14.8
a-NC_{500}	264.3	246.4	0.16	6.9	34.3	50.3	15.4
a-NC_{600}	456.4	431.0	0.26	6.3	29.7	54.4	15.9
a-NC_{700}	1302.4	979.0	0.76	4.5	23.9	56.3	19.8
a-NC_{800}	1548.4	1133.2	0.96	3.2	21.5	53.2	25.3

[a]Notation: S_{BET}, BET surface area; S_{micro}, micropore area; and V_{total}, total pore volume are calculated from N_2 sorption measurements; atomic N contents and N states are estimated from XPS and N 1s peak fitting.

which is presumably due to the cleavage of C−N rings and the rearrangement toward thermostable graphitic N, which is beneficial for a higher conductivity. The surface areas and porosities of NC and a-NCs are further revealed by N_2 sorption measurements. From Figure 3e, N_2 sorption of all samples demonstrate a combined I/IV type isotherm featured by a pronounced N_2 uptake at low relative pressure and a hysteresis loop in intermediate and high relative pressure region. The predominant type I curve at low relative pressure (below 0.1) with a quick N_2 filling evidence in the rich micropores, whereas at relative pressure of 0.2−1, the IV typed isotherms with H2 hysteresis loop indicates the coexistence of mesopores. From Table 1, the BET surface area of NC is 172 m^2 g^{-1}. By activation at lower temperatures, the BET surface areas are 264 and 456 m^2 g^{-1} for a-NC_{500} and a-NC_{600}, showing the limited increment in BET surface areas. Whereas undergoes activation at 700 and 800 °C, the specific surface areas of a-NC_{700} and a-NC_{800} enhance dramatically to 1302 and 1548 m^2 g^{-1}, respectively, suggesting the significance of activation temperature on the surface areas of a-NCs. NLDFT pore size distributions exhibit a series of micropores with width of 1−2 nm and small mesopores less than 7 nm (Figure 3f), showing the microporous and mesoporous texture of all samples. The micropore area ratios of NC, a-NC_{500}, a-NC_{600}, a-NC_{700}, and a-NC_{800} are 83, 93, 94, 75, and 73%, respectively. The high fraction of micropores in NC possibly stemmed from the cleaving of C−N bonds in MF resin and the discharging of evolved gases at carbonization temperature. The gradual increase of micropore area ratios for a-NCs shows that the activation at low temperature (below 600 °C) mainly creates micropores by etching of C−N matrix, while the etching at higher temperature mainly occurs onto the micropore wall and generate enhanced fraction of mesopores. Given the much higher BET surface areas and mesopore areas, a-NCs synthesized at higher activation temperature allows more efficient electrolyte diffusion and charge accumulation when employed as supercapacitor electrode. The compatibility of electrode surface to electrolyte is another factor crucial for charge accumulation and interface electrocatalytic reactions. To assess the wettability a-NCs to aqueous electrolyte, contact angles of NC and a-NC_{700} based supercapacitor electrodes were measured, from inset of Figure 3f, the water contact angle of NC is 68°, demonstrating the hydrophilic surface of NC due to the presence of rich N in the carbon matrix. In contrast, the contact angle lowers to 57° for a-NC_{700}, showing the increased wettability. The enhanced wettability is mainly ascribed to the increased surface O functionalities, which, accompanied by the N elemental, increase the surface polarity and hydrophilicity of a-NC_{700}. Additionally, the much rougher surface by alkali etching further reinforce this hydrophilicity,[35,36] thus offers better compatibility to aqueous or polar electrolyte and higher accessible surface area, therefore enhances the capacitive and photovoltaic performances when employed as supercapacitor and DSSC electrodes.

Electrochemical Properties in Supercapacitors. In view of the increased BET surface area with coexistence of

DOI: 10.1021/acsami.5b05790
ACS Appl. Mater. Interfaces 2015, 7, 20234−20244

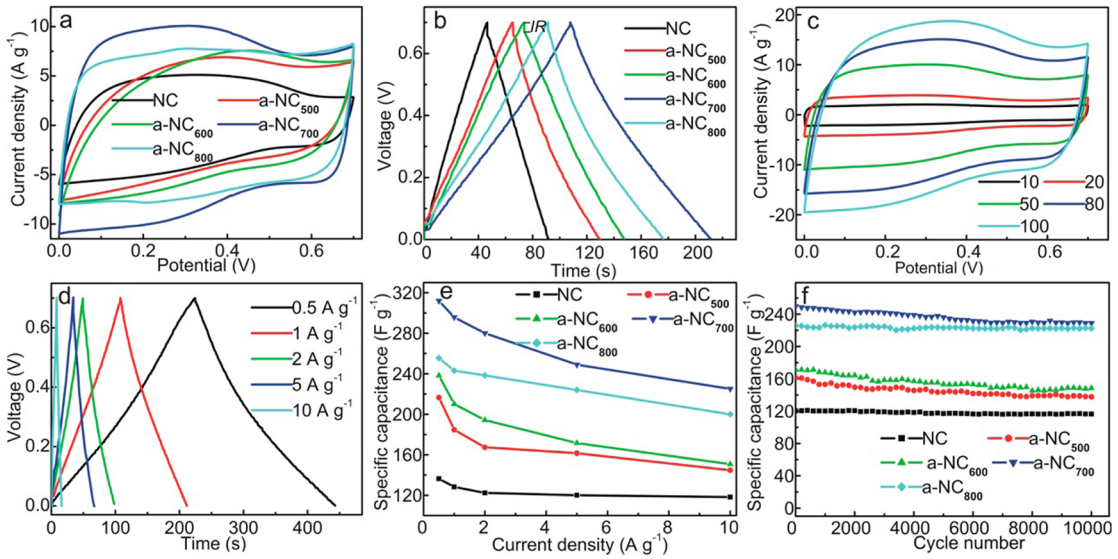

Figure 4. (a) CVs of NC and a-NCs in 1 M H_2SO_4 electrolyte at 50 mV s^{-1} in three-electrode configuration. (b) GCD curves of NC and a-NCs electrodes at current density of 1 A g^{-1} in double-electrode configuration. (c) CVs of a-NC_{700} electrode at various scan rates. (d) GCDs of a-NC_{700} electrode at different current densities. (e) Rate capabilities and (f) cycling performances of different electrodes at 5 A g^{-1}.

micropores and mesopores, the N-doped carbon framework with improved wettability, enhanced capacitive performances of a-NCs are envisaged. Figure 4a presents the CV curves of different electrodes in 0.1 M H_2SO_4 electrolyte in three-electrode configuration. Obviously, a nearly rectangular voltammogram profile with rapid current response at the reverse potential sweeping can be observed for all electrodes, showing the good EDL feature owing to the high surface area and charge/electrolyte ions conductivities.[26,37] In addition, a pair of reversible humps also appears for all electrodes, which is presumably derived from the reversible redox transformation of N and O functionalities;[38,39] it thus can offer a moderate fraction of pseudocapacitance. Relative to the NC, the capacitive currents of a-NCs enhance to different extents. The current densities and integrated areas surrounded by CV curves increase from a-NC_{500} to a-NC_{700}, whereas they slightly decrease for a-NC_{800}, indicating that the capacitance is not strictly increased with specific surface area of electrode material. A closer comparison of a-NC_{700} and a-NC_{800} shows that the higher capacitive current and loop area of the former is mainly caused by the higher redox current, suggesting the higher capacitance of a-NC_{700} is mainly derived from pseudocapacitance, which shows the contribution of pseudocapacitance to the overall capacitance of a-NCs. As it undergoes alkali activation, the increased BET surface area at high temperature renders the exposure of more N functionalities to electrolyte and causes the increase of both EDL capacitance and pseudocapacitance, which can be observed from the enhanced response current and the redox humps from a-NC_{500} to a-NC_{700}. Whereas for a-NC_{800}, although the BET surface is the highest, the pseudocapacitance declines obviously relative to a-NC_{700} due to the more severe N loss at higher temperature, which finally reduces the overall capacitance. Under activation temperature of 700 °C, the balanced EDL capacitance and pseudocapacitance results in the highest overall capacitance of a-NC_{700}. Figure 4b shows the typical GCD curves of different electrodes in double-electrode configuration. As seen, all the electrodes demonstrate similar charging−discharging profiles except the charging−discharging durations. The discharging durations of a-NCs are apparently longer than NC, reflecting the substantially improved capacitance by activation treatment. Additionally, the IR drop decreases relative to NC, showing the decreased electrolyte ions diffusion resistance by activation. As for a-NCs, the discharging duration increases obviously from a-NC_{500} to a-NC_{700}, which suggests the higher BET surface and more exposed N functionalities lead to the higher overall capacitance, whereas for a-NC_{800}, the shortened discharging duration relative to a-NC_{700} implies the lower capacitance. This trend coincides well with the CV tests.

Given the highest capacitance, capacitive performance of a-NC_{700} was further investigated. Figure 4c shows the CV curves of a-NC_{700} electrode at different scan rates, the capacitive current increases accordingly with potential scan rate. The CV shape and redox peaks can still be well-maintained at high scan rate; no obvious deformation of CV curve occurs at 100 mV s^{-1}, indicates the low IR at high scan rates because of the rich mesopores. At higher scan rates, the slightly increased overpotential is mainly derived from the unavoidable lag in current response for the insufficient electrolyte diffusion kinetics, which is common for the micropores containing electrode. Figure 4d displays the GCD curves of a-NC_{700} electrode at various current densities. The curves show almost symmetric charging−discharging profiles with low IR drop, showing the EDL capacitance and reversible redox of N and O functionalities. The enhanced IR at higher current density is attributed to the increased ions diffusion resistance within the micropores at high operation current density, which is consistent with the CV results. The slight deviation of the discharge branch from linearity indicates the coexistence of pseudocapacitance. C_ss of a-NC_{700} electrode calculated based on eq 1 are 312, 295.8, 280.1, 249, and 225.1 F g^{-1}, respectively, at current density of 0.5, 1, 2, 5, and 10 A g^{-1}, showing the high C_s in a wide range of current densities. The C_s at 1 A g^{-1} is higher over other MF-derived porous NC (220 F g^{-1}),[24] hollow sphere NCs (260 F g^{-1}),[25] hierarchical porous NC (~280 F g^{-1}),[26] graphene-incorporated NC xerogel (205 F g^{-1}),[40] as well as being higher over the ethylenediamine tetraacetic acid salt based NC (~260 F g^{-1})[41] and graphene-

DOI: 10.1021/acsami.5b05790
ACS Appl. Mater. Interfaces 2015, 7, 20234−20244

incorporated porous NC (~280 F g^{-1}),[42] whereas inferior to beer yeast cell based graphene–NC composite (308 F g^{-1}),[9] gelatin-derived porous NC (~320 F g^{-1}),[43] and phenolic resin based NC spheres (388 F g^{-1}).[34]

Figure 4e compares the rate capabilities of different electrodes; the C_s retentions within the current range of 0.5–10 A g^{-1} are 86.7, 66.8, 63.3, 72.1, and 78.3% for NC, a-NC_{500}, a-NC_{600}, a-NC_{700}, and a-NC_{800}, respectively. As for a-NCs, the rate capability increases at higher activation temperature for the decreased electrolyte diffusion resistance associate with higher fraction of mesopores, but in this current density range, C_ss of a-NC_{700} are apparently higher over its cousins, showing the advantageous capacitive performances in a wide range of current densities.

Figure 4f shows the cycling stabilities of different electrodes under 10 000 successive charging–discharging cycles at 5 A g^{-1}; C_s of a-NC_{700} gradually decays from 249.0 to 229.1 F g^{-1}, which accounts for 92.0% maintaining ratio of its initial value. The high cycling durability is mainly attributed to the chemical inertness of carbon matrix against electrolyte ions as well as the rapid and reversible redox transformations of surface N and O functionalities. The higher cycling stability of a-NC_{800} (99.3%) over a-NC_{700} is mainly due to the higher EDL capacitance contribution. C_s retention ratios of a-NC_{500} and a-NC_{600} are 85.2 and 86.5%, respectively, showing the excellent cycling stabilities of all a-NCs. The cycling stability of NC is also high (96.6%), but the low C_s limits its application in supercapacitor.

The C_s of the electrode material directly determines E_{cell} and P_{cell} of the resultant supercapacitor. Figure 5a shows Ragone

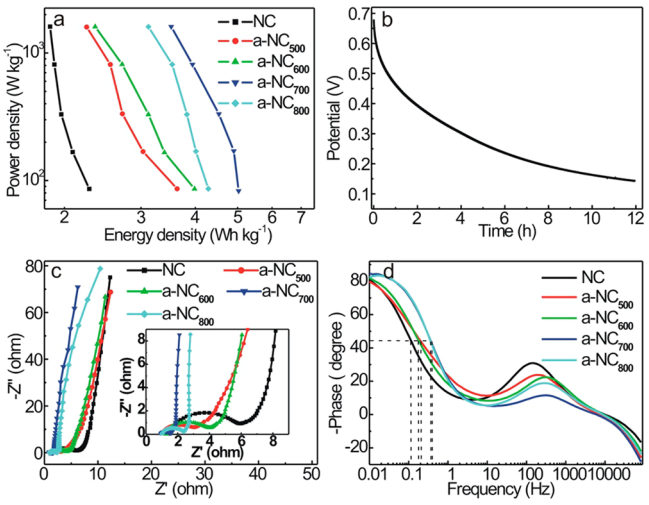

Figure 5. (a) Ragone plots of supercapacitors based on different electrodes. (b) Self-discharge curve of a-NC_{700} supercapacitor after being charged to 0.7 V. (c) Nyquist plots of the supercapacitor based on different electrodes; inset: enlarged region at high frequency. (d) Bode curve of impedance for different supercapacitors.

plots of supercapacitors based on different materials. E_{cell} and P_{cell} of a-NC_{700} device are 5.0 Wh kg^{-1} and 83 W kg^{-1} at 0.5 A g^{-1}, and E_{cell} decreases to 3.52 Wh kg^{-1} whereas P_{cell} increases to 1608.8 W kg^{-1} at 10 A g^{-1}. Within the similar P_{cell} range, E_{cell}'s of a-NC_{700} supercapacitor are apparently higher versus other devices, demonstrating the superior energy output performance. Given the highest C_s and E_{cell}, excellent rate capability and cycling stability, a-NC_{700} herein is believed to be a competitive electrode material of supercapacitor owing to the structural features including the high BET surface area, proper micropore and mesopore fractions, modest graphitization, and coexistence of pseudocapacitive N and O functionalities.

Figure 5b displays the self-discharging curve of fully charged a-NC_{700} supercapacitor; after 12 h of self-discharging, the open circuit voltage declines gradually to 0.14 V. From this self-discharging phenomenon, to minimize the undesired energy loss, our supercapacitor is suitable for application in complementary energy facilities without long-term self-discharging duration, such as uninterrupted power systems and hybrid power sources.

The resistance behavior of supercapacitor electrodes can be revealed by EIS measurement. From Figure 5c, Nyquist plots of NC and a-NCs supercapacitors comprise an arc at the high-frequency region and a straight line at the low-frequency end. The series resistance (R_s) can be directly estimated from the intercept on real axis at the high-frequency end; the R_s of a-NC_{700} (0.93 Ω) is slightly lower than those of other devices (1.50, 1.04, 1.27, and 1.00 Ω, respectively, for NC, a-NC_{500}, a-NC_{600}, and a-NC_{800}). The largely similar R_s values mainly derive from the same fraction of conductive carbon black in electrodes and the same ionic conductivity of electrolyte. The high-frequency arc represents the charge-transfer resistance (R_{ct}); the narrower arc radius of a-NC devices over their NC counterpart suggests the more sufficient electrolyte ions accumulation onto the electrode surface and the efficient redox reaction at a-NCs interface.[44,45] R_{ct} values of NC, a-NC_{500}, a-NC_{600}, a-NC_{700}, and a-NC_{800} are 1.72, 1.01, 1.38, 0.31, and 0.68 Ω, respectively. The lowest R_{ct} of a-NC_{700} suggests the most efficient accumulation of electrolyte ions onto the electrode surface and the rapid redox reaction at the electrode/electrolyte interface, which thus leads to the highest EDL and pseudocapacitance. At low frequencies, all devices exhibit almost a vertical line; the tail with a slope of 45° represents the Warburg diffusion resistance (Z_w),[44,45] the shorter length of this diffusion section in a-NC capacitors means lower ions diffusion resistances, which is mainly attributed to the higher mesopores fraction and the enhanced surface hydrophilicity. The nearly vertical trend at the low-frequency end for a-NCs shows the ideal EDL capacitance behavior as a result of the large accessible surface areas. In all, the lower R_s, R_{ct}, and Z_w make a-NCs efficient electrode materials for supercapacitor. To more comprehensively scrutinize the resistance of different devices, Bode plots of EIS were compared (Figure 5d); the phase angles of a-NC capacitors at the low-frequency end are more close to −90°, showing the ideal capacitive behavior. Moreover, the more distinct frequency responses of a-NC_{700} and a-NC_{800} supercapacitors at a phase angle of −45° indicate the lower Z_ws owing to the higher fractions of mesopores, which contribute to higher charging–discharging rates. The corresponding frequencies (f_0) at −45° are 0.12, 0.21, 0.18, 0.38, and 0.37 Hz, respectively, for NC, a-NC_{500}, a-NC_{600}, a-NC_{700}, and a-NC_{800}. As a result, the electron lifetimes (τ), calculated according to $\tau = 1/f_0$,[46,47] where the capacitive and resistive impedances are equal, are 8.3, 4.8, 5.6, 2.6, and 2.7 s for NC, a-NC_{500}, a-NC_{600}, a-NC_{700}, and a-NC_{800} supercapacitors. The shortest τ of a-NC_{700} capacitor indicates the most rapid charge accumulation and delivery at a-NC_{700} surface. Hence, a-NC_{700} herein is the most promising electrode material for efficient supercapacitor.

Due to the use of aqueous electrolyte, the output voltage of a single supercapacitor is limited in practical applications. To meet the operation voltage requirements, the output perform-

DOI: 10.1021/acsami.5b05790
ACS Appl. Mater. Interfaces 2015, 7, 20234–20244

ance should be tunable by assembling individual supercapacitors into supercapacitor arrays in different connecting modes. To evaluate the output performance of supercapacitor arrays, GCD curves of the supercapacitor arrays by direct connection of 4 identical supercapacitor units in series and/or in parallel configurations were measured. Figure 6a shows the

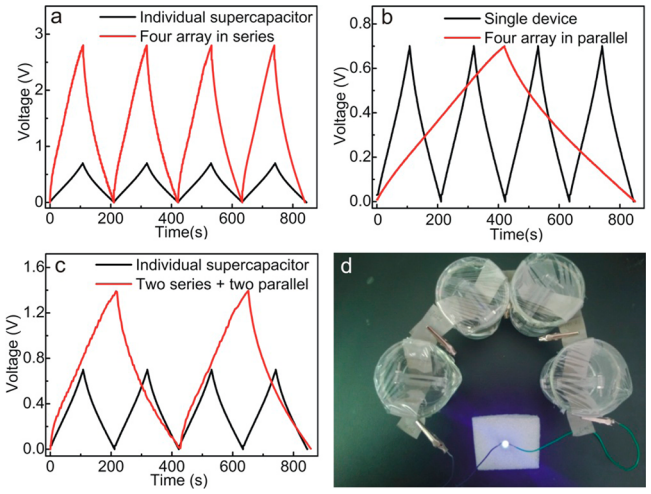

Figure 6. GCD curves of 4-supercapacitor arrays connected (a) in series, (b) in parallel, (c) 2 series + 2 parallel. (d) Photograph of a LED powered by 4-supercapacitor array in series.

GCD curves of the 4-supercapacitor array in series and individual unit at 1 A g^{-1}. In this supercapacitor array, the voltage is widened quadruple to 2.8 V; the GCD curve of the supercapacitor array shows similar charging−discharging profiles with imperceptible IR drop, which indicates the good capacitive properties with low internal resistance. Additionally, the discharging duration remains unvaried, showing almost 100% capacitance-maintaining ability in the supercapacitor array. When 4 identical supercapacitor units are connected in parallel and measured within the same voltage window (Figure 6b), the discharging duration of the supercapacitor array is 4 times longer relative to an individual unit, showing that the overall capacitance is 4 times higher than that for the individual unit, which also attests the good capacitive performance in parallel assembly. The 4 identical supercapacitor units are further connected by assembling 2 units in parallel followed by linking the 2 sets of arrays in series (2 series + 2 parallel); the 4-supercapacitor array shows doubled discharging duration under enlarged voltage of 1.4 V (Figure 6c). The almost equal overall capacitance also indicates the good capacitance-maintaining ability. The high capacitance-retaining abilities in different arrays validate the feasibility of assembling a-NC_{700} into amplified supercapacitor arrays according to voltage and power output requirement in practical applications. As a demonstration of the feasibility for practical application of a-NC_{700} supercapacitor, the 4-supercapacitor array in series is used to light up a light-emitting diode (LED) with positive working voltage of 2.4−2.8 V. After being charged to 2.8 V at 1 A g^{-1}, the supercapacitor array can sustain the lighting of LED for 12 min (Figure 6d), which visually shows the potential of a-NC_{700} supercapacitor in amplified applications.

Electrochemical Properties in Catalytic CE of DSSC. Because of the porous nature with moderate N doping level and the incorporation of graphene, a-NCs can offer efficient charge/ions diffusion channels, which are crucial for electrocatalysis reaction. Additionally, the lone-pair electrons of doped N in carbon matrix can serve as electron donors to boost the reduction of I_3^- in the internal circuit of DSSC; hence, a-NCs are expected to be efficient catalytic CE materials of DSSC. Herein, a-NC_{700} was employed as representative CE material to evaluate the catalytic activity on I_3^- reduction, and traditional thermally decomposed Pt electrode composing of stacked particles (inset in Figure 7c) was also measured as a

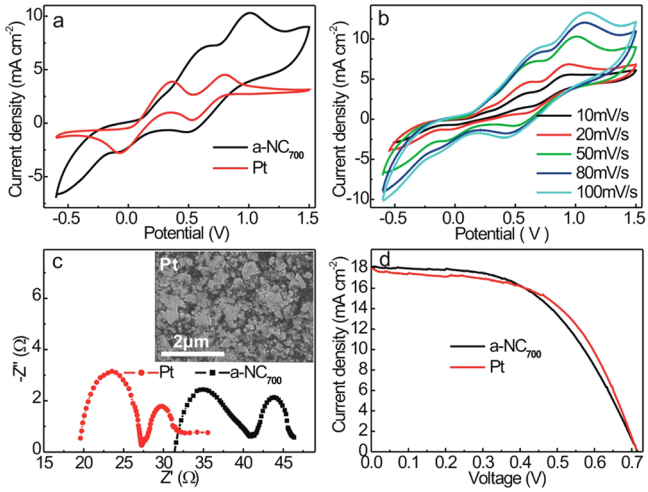

Figure 7. (a) CVs of a-NC_{700}/FTO and Pt/FTO electrodes in acetonitrile electrolyte containing 10 mM LiI, 1 mM I_2, and 0.1 M $LiClO_4$ at a scan rate of 50 mV/s. (b) CVs of a-NC_{700}/FTO electrode at different scan rates. (c) Nyquist plots of symmetrical cells based on a-NC_{700}/FTO and Pt/FTO electrodes, inset: SEM of Pt electrode. (d) *J*−*V* curves of DSSCs based on a-NC_{700}/FTO and Pt/FTO CEs under one-sun illumination (AM1.5).

comparison. Figure 7a shows the CVs of a-NC_{700} and Pt electrodes in iodide electrolyte; both electrodes demonstrate two pairs of redox peaks, which are indexed to the redox transformation of I_3^-/I^- and I_2/I_3^- redox pairs.[19] The electrocatalytic activity for I_3^- reduction can be reflected by the cathodic peak of the left pair. The classical Pt electrode arouses a well-defined cathodic peak at −0.06 V, showing the high catalytic activity for I_3^- reduction. Whereas for a-NC_{700} the redox peaks are not well-defined due to the existence of capacitive current, which is common for porous electrodes, but the wide cathodic peak located at −0.07 V can still be observed. The similar cathodic current and the wide peak width, viz. larger peak area of a-NC_{700} relative to Pt electrode, suggest the slightly higher catalytic activity for I_3^- reduction, whereas the peak separation between anodic and cathodic peaks of I_3^-/I^- pair for a-NC_{700} is larger than that for Pt, which means the lower conductivity of the former relative to metallic Pt. In view of the possibly high catalytic activity on I_3^- reduction, a-NC_{700} herein is also an efficient CE material for DSSC. Figure 7b shows CVs of a-NC_{700} electrode at various scan rates; the cathodic current increases accordingly with scan rate, indicating the reduction of I_3^- is controlled by the diffusion and the adsorption onto a-NC_{700} surface. The overpotential also increases with scan rate, which means the increased resistance for the insufficient I_3^- diffusion kinetics at higher scan rate; this phenomenon is similar to the rate performance in supercapacitor (Figure 4c). Albeit this, given the 0.3−0.6 nm diameter of I_3^- ion,[48] the high fraction of mesopores still can provide efficient electrolyte ion-diffusion channels to access the

DOI: 10.1021/acsami.5b05790
ACS Appl. Mater. Interfaces 2015, 7, 20234−20244

deep interior micropores and subject it to catalytic reduction; the decreased inner circuit resistance is beneficial for an acceptable filling factor (FF).

To gain further insight into the interfacial electrochemical behavior of a-NC_{700} CE, EISs of symmetric cells based on a-NC_{700} and Pt CEs were measured and compared. From Figure 7c, Nyquist plots of both devices include two distinct semicircles at high- and low-frequency regions. The impedance of CE commonly comprises intrinsic R_s of CE (at ∼100 kHz), R_{ct} at CE/electrolyte interface (∼1−100 kHz), and Z_w of electrolyte (0.1−10 Hz).[49−51] R_s of Pt and a-NC_{700} are estimated to be 19.6 and 31.3 Ω, respectively. The apparently larger R_s of a-NC_{700} is due to the intrinsically lower conductivity of a-NC_{700} over metallic Pt and the less effective electron propagation paths within the highly porous texture. R_{ct} of Pt and a-NC_{700} electrodes are 7.7 and 7.5 Ω, respectively; the slightly lower R_{ct} of the latter reflects the higher catalytic activity for I_3^- reduction, which coincides with the CV results. Z_w of the two electrodes are 5.0 and 4.9 Ω, respectively, which shows the similar electrolyte diffusion kinetics. Given the faint discrepancy in R_{ct} and Z_w, the higher R_s of a-NC_{700} means the higher overall inner circuit resistance relative to Pt, which will cause relatively lower FF of the pertinent DSSC.

Figure 7d presents the $J-V$ curves of DSSCs based on a-NC_{700} and Pt CEs; it can be observed that both cells demonstrate the same open circuit voltage (V_{oc}) of 0.72 V, so the difference in PCE mainly derives from the photocurrent density (J_{sc}) and FF. The DSSC based on Pt CE offers a J_{sc} of 17.92 mA cm^{-2} and a FF of 0.55; therefore, a PCE of 7.10% is achieved. The J_{sc} of a-NC_{700} based cell enhances slightly to 18.11 mA cm^{-2}, whereas FF (0.53) is a little lower. The slightly higher J_{sc} is mainly attributed to the slightly higher catalytic activity on I_3^- reduction by virtue of the highly accessible surface area, which can be observed from the slightly larger cathodic peak area in the CV curve (Figure 7a). In contrast, the lower FF of a-NC_{700} cell mainly stemmed from the larger R_s versus that for Pt, which is universal for carbon CEs. Albeit this, a PCE of 6.91% can still be offered for a-NC_{700} based cell, which is comparable to that for Pt. The PCE of a-NC_{700} CE based cell is comparable to those for other NC-based devices.[10,11,18,19,52] Considering the obvious cost advantage, a-NC_{700} herein is also a competitive Pt-free catalytic CE material in DSSC.

4. CONCLUSIONS

In summary, a-NCs were synthesized by carbonization and activation of chemically bridged G-MF resin composite precursor. The high BET surface area and moderate N doping level make a-NC_{700} an efficient electrode material for supercapacitor with high capacitance, rate capability, and cycling stability. The output voltage can be further tuned by assembling supercapacitor arrays in different connection forms, demonstrating the potential of a-NC_{700} in amplified applications. Moreover, the porous texture and N doping also benefits a high catalytic activity on reduction of iodide mediator in electrolyte of DSSC. When a-NC_{700} was used as CE of DSSC, the PCE of pertinent DSSC is comparable to that for its Pt-based counterpart. The excellent capacitive and photovoltaic performances highlight the bright prospect of a-NCs in sustainable energy devices.

AUTHOR INFORMATION

Corresponding Authors

*E-mail: zygao512@163.com. Tel./Fax: +86 373 3326209.
*E-mail: kjiang512@163.com. Tel./Fax: +86 373 3326209.

Notes

The authors declare no competing financial interest.

ACKNOWLEDGMENTS

This work was supported by National Science Foundation of China (nos. 61204078, 61176004, and U1304505), Program for Innovative Research Team and Talent (in Science and Technology) in University of Henan Province (nos. 13IRTSTHN026 and 15HASTIT006), and Innovation Scientists and Technicians Troop Construction Projects of Henan Province (154200510009).

REFERENCES

(1) Wei, L.; Sevilla, M.; Fuertes, A. B.; Mokaya, R.; Yushin, G. Hydrothermal Carbonization of Abundant Renewable Natural Organic Chemicals for High Performance Supercapacitor Electrodes. *Adv. Energy Mater.* **2011**, *1*, 356−361.

(2) Liou, T. H. Development of Mesoporous Structure and High Adsorption Capacity of Biomass-Based Activated Carbon by Phosphoric Acid and Zinc Chloride Activation. *Chem. Eng. J.* **2010**, *158*, 129−142.

(3) Yang, X.; Cheng, C.; Wang, Y.; Qiu, L.; Li, D. Liquid-Mediated Dense Integration of Graphene Materials for Compact Capacitive Energy Storage. *Science* **2013**, *341*, 534−537.

(4) Han, S.; Wu, D. Q.; Li, S.; Zhang, F.; Feng, X. L. Porous Graphene Materials for Advanced Electrochemical Energy Storage and Conversion Devices. *Adv. Mater.* **2014**, *26*, 849−864.

(5) Zhu, Y. W.; Murali, S.; Stoller, M. D.; Ganesh, K. J.; Cai, W. W.; Ferreira, P. J.; Pirkle, A.; Wallace, R. M.; Cychosz, K. A.; Thommes, M.; Su, D.; Stach, E. A.; Ruoff, R. S. Carbon-Based Supercapacitors Produced by Activation of Graphene. *Science* **2011**, *332*, 1537−1541.

(6) Xiao, X.; Li, T. Q.; Peng, Z. H.; Jin, H. Y.; Zhong, Q. Z.; Hu, Q. Y.; Yao, B.; Luo, Q. P.; Zhang, C. F.; Gong, L.; Chen, J.; Gogotsi, Y.; Zhou, J. Freestanding Functionalized Carbon Nanotube-Based Electrode for Solid-State Asymmetric Supercapacitors. *Nano Energy* **2014**, *6*, 1−9.

(7) Zhai, Y.; Dou, Y.; Zhao, D.; Fulvio, P. F.; Mayes, R. T.; Dai, S. Carbon Materials for Chemical Capacitive Energy Storage. *Adv. Mater.* **2011**, *23*, 4828−4850.

(8) Hulicova-Jurcakova, D.; Kodama, M.; Shiraishi, S.; Hatori, H.; Zhu, Z. H.; Lu, G. Q. Nitrogen-Enriched Nonporous Carbon Electrodes with Extraordinary Supercapacitance. *Adv. Funct. Mater.* **2009**, *19*, 1800−1809.

(9) Yuanyuan, Y.; Ruiyi, L; Zaijun, L.; Junkang, l.; Zhiguo, G.; Guangli, W. A Facile Self-Template Strategy to Fabricate Three-Dimensional Nitrogen-Doped Hierarchical Porous Carbon/Graphene for Conductive Agent-Free Supercapacitors with Excellent Electrochemical Performance. *Electrochim. Acta* **2014**, *125*, 330−337.

(10) Yang, D.-S.; Kim, C.; Song, M. Y.; Park, H.-Y.; Kim, J. C.; Lee, J.-J.; Ju, M. J.; Yu, J.-S. N-Doped Hierarchical Hollow Mesoporous Carbon as Metal-Free Cathode for Dye-Sensitized Solar Cells. *J. Phys. Chem. C* **2014**, *118*, 16694−16702.

(11) Xue, Y.; Liu, J.; Chen, H.; Wang, R.; Li, D.; Qu, J.; Dai, L. Nitrogen-Doped Graphene Foams as Metal-Free Counter Electrodes in High-Performance Dye-Sensitized Solar Cells. *Angew. Chem., Int. Ed.* **2012**, *51*, 12124−12127.

(12) Kong, X.-K.; Sun, Z.-y.; Chen, M.; Chen, C.-l.; Chen, Q.-w. Metal-Free Catalytic Reduction of 4-Nitrophenol to 4-Aminophenol by N-Doped Graphene. *Energy Environ. Sci.* **2013**, *6*, 3260−3266.

(13) Sun, H.; Wang, Y.; Liu, S.; Ge, L.; Wang, L.; Zhu, Z.; Wang, S. Facile Synthesis of Nitrogen Doped Reduced Graphene Oxide as a Superior Metal-Free Catalyst for Oxidation. *Chem. Commun.* **2013**, *49*, 9914−9916.

DOI: 10.1021/acsami.5b05790
ACS Appl. Mater. Interfaces 2015, 7, 20234−20244

(14) Gao, Y.; Hu, G.; Zhong, J.; Shi, Z.; Zhu, Y.; Su, D. S.; Wang, J.; Bao, X.; Ma, D. Nitrogen-Doped sp^2-Hybridized Carbon as a Superior Catalyst for Selective Oxidation. *Angew. Chem., Int. Ed.* **2013**, *52*, 2109−2113.
(15) Yang, Z.; Nie, H.; Chen, X.; Chen, X.; Huang, S. Recent Progress in Doped Carbon Nanomaterials as Effective Cathode Catalysts for Fuel Cell Oxygen Reduction Reaction. *J. Power Sources* **2013**, *236*, 238−249.
(16) Ju, M. J.; Kim, J. C.; Choi, H.-J.; Choi, I. T.; Kim, S. G.; Lim, K.; Ko, J.; Lee, J.-J.; Jeon, I.-Y.; Baek, J.-B.; Kim, H. K. N-Doped Graphene Nanoplatelets as Superior Metal-Free Counter Electrodes for Organic Dye-Sensitized Solar Cells. *ACS Nano* **2013**, *7*, 5243−5250.
(17) Wang, G.; Xing, W.; Zhuo, S. Nitrogen-Doped Graphene as Low-Cost Counter Electrode for High-Efficiency Dye-Sensitized Solar Cells. *Electrochim. Acta* **2013**, *92*, 269−275.
(18) Wang, G.; Kuang, S.; Wang, D.; Zhuo, S. Nitrogen-Doped Mesoporous Carbon as Low-Cost Counter Electrode for High-Efficiency Dye-Sensitized Solar Cells. *Electrochim. Acta* **2013**, *113*, 346−353.
(19) Zhai, P.; Wei, T.-C.; Chang, Y.-H.; Huang, Y- T.; Yeh, W.-T.; Su, H.; Feng, S.-P. High Electrocatalytic and Wettable Nitrogen-Doped Microwave-Exfoliated Graphene Nanosheets as Counter Electrode for Dye-Sensitized Solar Cells. *Small* **2014**, *10*, 3347−3353.
(20) Zhou, J.; Zhu, T.; Xing, W.; Li, Z.; Shen, H.; Zhuo, S. Activated Polyaniline-Based Carbon Nanoparticles for High Performance Supercapacitors. *Electrochim. Acta* **2015**, *160*, 152−159.
(21) Xing, Y.; Zheng, X.; Wu, Y.; Li, M.; Zhang, W.-H.; Li, C. Nitrogen-Doped Carbon Nanotubes with Metal Nanoparticles as Counter Electrode Materials for Dye-Sensitized Solar Cells. *Chem. Commun.* **2015**, *51*, 8146−8149.
(22) Yan, Y.; Kuila, T.; Kim, N. H.; Lee, S. H.; Lee, J. H. N-Doped Carbon Layer Coated Thermally Exfoliated Graphene and Its Capacitive Behavior in Redox Active Electrolyte. *Carbon* **2015**, *85*, 60−71.
(23) Zheng, X.; Deng, J.; Wang, N.; Deng, D.; Zhang, W.-H.; Bao, X.; Li, C. Podlike N-Doped Carbon Nanotubes Encapsulating FeNi Alloy Nanoparticles: High-Performance Counter Electrode Materials for Dye-Sensitized Solar Cells. *Angew. Chem., Int. Ed.* **2014**, *53*, 7023−7027.
(24) Jiang, J.; Bao, L.; Qiang, Y.; Xiong, Y.; Chen, J.; Guan, S.; Chen, J. Sol-Gel Process-Derived Rich Nitrogen-Doped Porous Carbon through KOH Activation for Supercapacitors. *Electrochim. Acta* **2015**, *158*, 229−236.
(25) Ma, F.; Zhao, H.; Sun, L.; Li, Q.; Huo, L.; Xia, T.; Gao, S.; Pang, G.; Shi, Z.; Feng, S. A Facile Route for Nitrogen-Doped Hollow Graphitic Carbon Spheres with Superior Performance in Supercapacitors. *J. Mater. Chem.* **2012**, *22*, 13464−13468.
(26) Li, T.; Yang, G.; Wang, J.; Zhou, Y.; Han, H. Excellent Electrochemical Performance of Nitrogen-Enriched Hierarchical Porous Carbon Electrodes Prepared Using Nano-$CaCO_3$ as Template. *J. Solid State Electrochem.* **2013**, *17*, 2651−2660.
(27) Gao, Z.; Wang, F.; Chang, J.; Wu, D.; Wang, X.; Wang, X.; Xu, F.; Gao, S.; Jiang, K. Chemically Grafted Graphene−Polyaniline Composite for Application in Supercapacitor. *Electrochim. Acta* **2014**, *133*, 325−334.
(28) Merline, D. J.; Vukusic, S.; Abdala, A. A. Melamine Formaldehyde: Curing Studies and Reaction Mechanism. *Polym. J.* **2013**, *45*, 413−419.
(29) Zhong, X.; Zhang, H.; Liu, S.; Deng, C.; Wang, M. Nitrogen-Enriched Carbon from Melamine Resins with Superior Oxygen Reduction Reaction Activity. *ChemSusChem* **2013**, *6*, 807−812.
(30) Hu, C.; Xiao, Y.; Zhao, Y.; Chen, N.; Zhang, Z.; Cao, M.; Qu, L. Highly Nitrogen-Doped Carbon Capsules: Scalable Preparation and High-Performance Applications in Fuel Cells and Lithium Ion Batteries. *Nanoscale* **2013**, *5*, 2726−2733.
(31) Liu, J.; Webster, S.; Carroll, D. L. Temperature and Flow Rate of NH_3 Effects on Nitrogen Content and Doping Environments of Carbon Nanotubes Grown by Injection CVD Method. *J. Phys. Chem. B* **2005**, *109*, 15769−15774.
(32) Peng, C.; Yan, X.-b.; Wang, R.-t.; Lang, J.-w.; Ou, Y.-j.; Xue, Q.-j. Promising Activated Carbons Derived from Waste Tea-Leaves and Their Application in High Performance Supercapacitors Electrodes. *Electrochim. Acta* **2013**, *87*, 401−408.
(33) Jansen, R. J. J.; van Bekkum, H. XPS of Nitrogen-Containing Functional Groups on Activated Carbon. *Carbon* **1995**, *33*, 1021−1027.
(34) Wickramaratne, N. P.; Xu, J.; Wang, M.; Zhu, L.; Dai, L.; Jaroniec, M. Nitrogen Enriched Porous Carbon Spheres: Attractive Materials for Supercapacitor Electrodes and CO_2 Adsorption. *Chem. Mater.* **2014**, *26*, 2820−2828.
(35) Burton, Z.; Bhushan, B. Hydrophobicity, Adhesion, and Friction Properties of Nanopatterned Polymers and Scale Dependence for Micro- and Nanoelectromechanical Systems. *Nano Lett.* **2005**, *5*, 1607−1613.
(36) Chang, J.; Gao, Z.; Wang, X.; Wu, D.; Xu, F.; Wang, X.; Guo, Y.; Jiang, K. Activated Porous Carbon Prepared from Paulownia Flower for High Performance Supercapacitor Electrodes. *Electrochim. Acta* **2015**, *157*, 290−298.
(37) Xing, W.; Qiao, S. Z.; Ding, R. G.; Li, F.; Lu, G. Q.; Yan, Z. F.; Cheng, H. M. Superior Electric Double Layer Capacitors Using Ordered Mesoporous Carbons. *Carbon* **2006**, *44*, 216−224.
(38) Frackowiak, E. Carbon Materials for Supercapacitor Application. *Phys. Chem. Chem. Phys.* **2007**, *9*, 1774−1785.
(39) Rufford, T. E.; Hulicova-Jurcakova, D.; Zhu, Z. H.; Lu, G. Q. Nanoporous Carbon Electrode from Waste Coffee Beans for High Performance Supercapacitors. *Electrochem. Commun.* **2008**, *10*, 1594−1597.
(40) Lei, G.; Hu, X.; Peng, Z.; Hu, J.; Liu, H. Facile Synthesis of Reduced Graphene Oxide-Modified, Nitrogen-Doped Carbon Xerogel with Enhanced Electrochemical Capacitance. *Mater. Chem. Phys.* **2014**, *148*, 1171−1177.
(41) Xu, B.; Duan, H.; Chu, M.; Cao, G.; Yang, Y. Facile Synthesis of Nitrogen-Doped Porous Carbon for Supercapacitors. *J. Mater. Chem. A* **2013**, *1*, 4565−4570.
(42) Jin, Z.-Y.; Lu, A.-H.; Xu, Y- Y.; Zhang, J.-T.; Li, W.-C. Ionic Liquid-Assisted Synthesis of Microporous Carbon Nanosheets for Use in High Rate and Long Cycle Life Supercapacitors. *Adv. Mater.* **2014**, *26*, 3700−3705.
(43) Xu, B.; Hou, S.; Cao, G.; Wu, F.; Yang, Y. Sustainable Nitrogen-Doped Porous Carbon with High Surface Areas Prepared from Gelatin for Supercapacitors. *J. Mater. Chem.* **2012**, *22*, 19088−19093.
(44) Sun, L.; Tian, C.; Fu, Y.; Yang, Y.; Yin, J.; Wang, L.; Fu, H. Nitrogen-Doped Porous Graphitic Carbon as an Excellent Electrode Material for Advanced Supercapacitors. *Chem. - Eur. J.* **2014**, *20*, 564−574.
(45) Puthusseri, D.; Aravindan, V.; Madhavi, S.; Ogale, S. 3D Microporous Conducting Carbon Beehive by Single Step Polymer Carbonization for High Performance Supercapacitors: The Magic of In Situ Porogen Formation. *Energy Environ. Sci.* **2014**, *7*, 728−735.
(46) Wang, D.; Min, Y.; Yu, Y.; Peng, B. A General Approach for Fabrication of Nitrogen-Doped Graphene Sheets and Its Application in Supercapacitors. *J. Colloid Interface Sci.* **2014**, *417*, 270−277.
(47) Wu, Z.-S.; Parvez, K.; Feng, X.; Müllen, K. Graphene-Based In-Plane Micro-supercapacitors with High Power and Energy Densities. *Nat. Commun.* **2013**, *4*, 2487.
(48) Lee, W. J.; Ramasamy, E.; Lee, D. Y.; Song, J. S. Efficient Dye-Sensitized Solar Cells with Catalytic Multiwall Carbon Nanotube Counter Electrodes. *ACS Appl. Mater. Interfaces* **2009**, *1*, 1145−1149.
(49) Hauch, A.; Georg, A. Diffusion in the Electrolyte and Charge-Transfer Reaction at the Platinum Electrode in Dye-Sensitized Solar Cells. *Electrochim. Acta* **2001**, *46*, 3457−3466.
(50) Sun, H.; Luo, Y.; Zhang, Y.; Li, D.; Yu, Z.; Li, K.; Meng, Q. In Situ Preparation of a Flexible Polyaniline/Carbon Composite Counter Electrode and Its Application in Dye-Sensitized Solar Cells. *J. Phys. Chem. C* **2010**, *114*, 11673−11679.
(51) Duan, X.; Gao, Z.; Chang, J.; Wu, D.; Ma, P.; He, J.; Xu, F.; Gao, S.; Jiang, K. CoS_2-Graphene Composite as Efficient Catalytic Counter

DOI: 10.1021/acsami.5b05790
ACS Appl. Mater. Interfaces 2015, 7, 20234−20244

Electrode for Dye-Sensitized Solar Cell. *Electrochim. Acta* **2013**, *114*, 173−179.
(52) Song, L.; Luo, Q.; Zhao, F.; Li, Y.; Lin, H.; Qu, L.; Zhang, Z. Dually Functional, N-Doped Porous Graphene Foams as Counter Electrodes for Dye-Sensitized Solar Cells. *Phys. Chem. Chem. Phys.* **2014**, *16*, 21820−21826.

DOI: 10.1021/acsami.5b05790
ACS Appl. Mater. Interfaces 2015, 7, 20234−20244